IJNAOE
©SNAK, 2015

Int. J. Nav. Archit. Ocean Eng. (2015) 7:346~363
http://dx.doi.org/10.1515/ijnaoe-2015-0024
pISSN: 2092-6782, eISSN: 2092-6790

Integrated dynamics modeling for supercavitating vehicle systems

Seonhong Kim and Nakwan Kim

Department of Naval Architecture and Ocean Engineering, Seoul National University, Seoul, Korea

ABSTRACT: *We have performed integrated dynamics modeling for a supercavitating vehicle. A 6-DOF equation of motion was constructed by defining the forces and moments acting on the supercavitating body surface that contacted water. The wetted area was obtained by calculating the cavity size and axis. Cavity dynamics were determined to obtain the cavity profile for calculating the wetted area. Subsequently, the forces and moments acting on each wetted part-the cavitator, fins, and vehicle body-were obtained by physical modeling. The planing force-the interaction force between the vehicle transom and cavity wall-was calculated using the apparent mass of the immersed vehicle transom. We integrated each model and constructed an equation of motion for the supercavitating system. We performed numerical simulations using the integrated dynamics model to analyze the characteristics of the supercavitating system and validate the modeling completeness. Our research enables the design of high-quality controllers and optimal supercavitating systems.*

KEY WORDS: Supercavitating vehicle; Integrated dynamics modeling; Supercavity; 6-DOF equation of motion; Planing force; Cavity dynamics; Frictional drag force; Cavity bubble; Cavity model; Open-loop numerical simulation.

INTRODUCTION

Objects moving in fluid media such as water are slowed down by fluid forces that are collectively called drag. Drag forces increase quadradically with the object speed, and hence, the thrust force also increases. Therefore, underwater vehicles have a velocity limit due to the limit of thrust force.

Numerous researches have been conducted to reduce the drag and increase the speed of underwater vehicles. In the 1970s, Russian scientists proposed a radically different approach to solve this problem; they proposed reductions in the surface area of the body that is in contact with water to eliminate one type of drag, the skin-friction drag. When an object moves fast in water, an air bubble called "cavity" is formed. The supercavitating technology, proposed by the Russians, is based on the idea that skin-friction drag can be reduced dramatically when a vehicle is encompassed by large gas bubbles. A supercavitating vehicle changes from fully wetted condition to supercavitating condition, and this causes unsteady hydrodynamical forces and moments because the wetted area of the vehicle body changes. The wetted area of the vehicle body is determined by the shape of the cavity and the relative position between the cavity and vehicle. Therefore, the most important task is to calculate the cavity size and axis. If cavity modeling is successfully completed, the wetted part of the vehicle can be determined and it becomes possible to calculate the forces and moments acting on the vehicle body and control surface.

Many scientists have studied the dynamics and characteristics of the supercavitating vehicle, but their studies have been

Corresponding author: *Nakwan Kim*, e-mail: *nwkim@snu.ac.kr*

limited to specific areas and their models do not encompass the entire supercavitating system. In recent years, efforts have been made to study the dynamics of the supercavitating vehicle in various applications. In these investigations, one research focus has been the modeling of the system dynamic under fully developed cavitating conditions; control problems have also been investigated. Dzielski and Kurdila (2003) have researched the modeling and control problem in the early development phase. The longitudinal dynamics and control problem have been studied by Vanek (2007), Dzielski (2011), and Fan et al. (2011). Li et al. (2014) and Nguyen et al. developed a vertical plane model incorporated with time-delay effect. Hassouneh et al. (2013) developed a dive-plane model with noncylindrical and nonsymmetric cavity shape. Studies on supercavitating flow have also been conducted; early researches into the partial cavitation flow of axisymmetric bodies using a steady potential-flow boundary-element technique were performed by Varghese et al. (2005). Ahn et al. (2012) studied the supercavitating flows around a cavitator for various two and three dimensional shapes. Park and Rhee (2012) studied a high-speed super-cavitating flow around a two-dimensional symmetric wedge-shaped cavitator using an unsteady Reynolds-averaged Navier-Stokes equations solver based on a cell-centered finite volume method. Recently, numerical approaches for a ventilated partial cavity in the transition phase have been investigated. Zou et al. (2010) established an empirical formula for the gas-leakage rate of an unsteady ventilated supercavity using the nonlinear least square method based on the mass balance equation; the results of numerical simulations were then compared with the results from experiments. Additionally, Xiang et al. (2011) reported a numerical study on the drag reduction mechanism created by a ventilated partial cavity. Elbing et al. (2008) studied the plate skin-friction drag reduction caused by air bubbles; they tested the drag reduction by injecting gas from the line source so that there are two distinct drag-reduction phenomena: bubble drag reduction and air-layer drag reduction.

In this study, we have constructed a 6-DOF equation of motion for a supercavitating vehicle system. To define the forces and moments acting on the vehicle body, the supercavitating vehicle system was divided into cavitator, fins, and vehicle body. Each part was modeled on the basis of previous researches, and we integrated them to define the dynamics of the supercavitating system. In the modeling part, we defined all the terms included in the 6-DOF equation of motion. After the mathematical model was constructed, we performed open-loop numerical simulations. In this paper, all the terms are first described and defined. Subsequently, we explain the calculations of the forces/moments and construct the mathematical model. Finally, by using the numerical simulation results, the physical characteristics of the supercavitating vehicle are analyzed and the modeling completeness is validated.

The main contribution of this study is integrated modeling of a 6-DOF supercavitating vehicle from partially cavitating condition at low speed to supercavitating condition at high speed including transition phase. The model of a supercavitating vehicle consists of every component of the dynamics such as cavity, cavitator, body, fins, and planing, and accommodates coupled motion between the longitudinal and the lateral dynamics. The modeling of cavity includes cavity dynamics with variation of the depth and the speed of the vehicle, the effect of time-delay, and the deformation of cavity axis due to the gravity effect which generates asymmetric drag forces on rudders and creates in turn oscillatory pitching motion. A descriptiton of hydrostatic and hydrodynamic force and moment applied on the wetted body is included in the modeling which is pivotal in proper modeling of the vehicle in the transition phase. In the case of partial cavity, the hydrostatic and hydrodynamaic force and moment acting on the wetted body depend on how much and which direction the vehicle is in contact with water. The direction and the depth of immersion are determined by relative geometry of the vehicle and the cavity with the time delay effect, which allows planing to arise in any radial direction of the vehicle. The integrated modeling of a supercavitating vehicle is expected to be used as a test-bed for a design of controller or an optimization of configurations of a supercavitating vehicle.

MODELING OF SUPERCAVITATING VEHICLE

6-DOF equation of motion

The cavitator is located at the fore body of the vehicle, and a disk and four fins are located at the aft in the shape of a cross (+), as shown in Fig. 1. We selected two coordinate systems, the earth-fixed coordinate system $O_E - X_E Y_E Z_E$ and body-fixed coordinate system $O_B - X_B Y_B Z_B$, as shown in Fig. 1. The origin of the earth-fixed coordinate system was at sea level (zero) while the origin of the body-fixed coordinate system was located at the center of gravity.

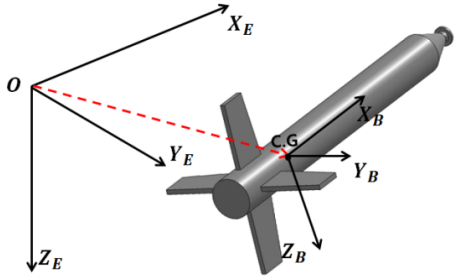

Fig. 1 Supercavitating vehicle.

The forces and moments acting on the vehicle are generated by the four fins, cavitator, gravity, thruster, wetted area of the body, and planing. The nonlinear equations of the supercavitating vehicle can be derived by using the linear momentum and angular momentum equations.

$$\begin{aligned} M\begin{bmatrix} \dot{u}+qw-vr \\ \dot{v}+ur-pw \\ \dot{w}+pv-uq \end{bmatrix} &= F_{Thrust}+F_{Cavitator}+F_{Fins}+F_{gravity}+F_{wet}+F_{Planing} \\ \begin{bmatrix} I_x\dot{p}+qr(I_z-I_y) \\ I_y\dot{q}+qr(I_x-I_z) \\ I_z\dot{r}+pq(I_y-I_x) \end{bmatrix} &= M_{Cavitator}+M_{Fins}+M_{wet}+M_{Planing} \end{aligned} \tag{1}$$

Here, (u,v,w) are the linear velocities during the surge, sway, and heave motions, and (p,q,r) are the angular velocities during the roll, pitch, and yaw motions. In this paper, it is assumed that the thrust force is acting only in the X_B-direction with magnitude T.

$$F_{Thrust}=T\times\begin{bmatrix}1\\0\\0\end{bmatrix} \tag{2}$$

Cavity model

The cavity is a major component of the supercavitating system. The behavior of the cavity bubble around the vehicle affects the fins and body immersion. The cavitator continuously creates the cavity while the vehicle is moving. The cavity axis, which is integration of each cavity section center, is equal to the trajectory of the cavitator, if there is no gravity effect and the cavitator angle of attack is zero; in other words, the cavity is axisymmetric. The plane that is perpendicular to the trajectory of the cavitator is called the cavity section and the cavity contour is obtained by integrating all the cavity sections along the trajectory of the cavitator. The cavity changes with time independent of the vehicle dynamics. Each cavity section first expands until it reaches its maximum radius and then starts to contract and disappear (Fig. 2).

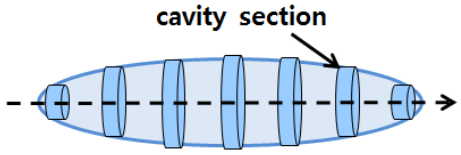

Fig. 2 Axisymmetric cavity and cavity sections.

The important parameter that represents the cavity characteristics is the cavitation number σ :

$$\sigma = \frac{p_\infty - p_c}{0.5\rho V^2} \tag{3}$$

p_∞ is the ambient pressure and p_c is the pressure inside the cavity measured in Pa; V is the vehicle velocity. The cavitation number σ is used to characterize the potential of the flow to cavitate. When σ is low and the velocity of the vehicle is fast or the cavity pressure is high, large and wide cavities tend to occur. Numerous studies have investigated cavity shape models; for example, Logvinovich (1972) studied the cavity radius and cavity contraction rate for the disk type cavitator in steady flow. Two numeric constants are defined to represent the cavity model:

$$k_1 = \frac{L}{R_n}\left(\frac{1.92}{\sigma_c} - 3\right)^{-1} - 13 \tag{4}$$

$$k_2 = \left(1 - \left(1 - \frac{4.5\sigma}{1+\sigma}\right)k_1^{(40/17)}\right)^{0.5} \tag{5}$$

The formula for the radius of the cavity at a distance L from the cavitator is

$$R_c = R_n\left(0.82\frac{(1+\sigma)}{\sigma}\right)^{0.5} k_2 \tag{6}$$

and the cavity contraction rate $\dot{R}_c$ is

$$\dot{R}_c = -\frac{20}{17}\left(0.82\frac{1+\sigma}{\sigma}\right)^{0.5} V\left(1 - \frac{4.5\sigma}{1+\sigma}\right)k_1^{(23/17)} \Big/ \left(k_2\left(\frac{1.92}{\sigma} - 3\right)\right) \tag{7}$$

The proposed formulae for the cavity shape are valid only if the following inequality is satisfied:

$$L > R_n\left(\frac{1.92}{\sigma} - 3\right) \tag{8}$$

To represent the frontal part of the cavity wherein the inequality is not satisfied, the following empirical formula is usually used (Logvinovich, 1972):

$$\frac{R}{R_n} = \left(1 + \frac{3x}{R_n}\right)^{1/3}, \quad \text{when } x < L \tag{9}$$

The formulae of Garabedian (1956) are useful for predicting the cavity length L_c and the maximum cavity radius $R_{\max}$:

$$\frac{L_c}{2R_n} = \frac{1}{\sigma}\sqrt{C_D \ln\frac{1}{\sigma}} \tag{10}$$

$$\frac{R_{\max}}{R_n} = \sqrt{\frac{C_D}{\sigma}} \tag{11}$$

C_D is the cavitator drag coefficient. The cavity profile can then be estimated by May's formula (May, 1975) as follows:

$$R_c(x) = R_{\max}\left(1-\left(\frac{x-L_c/2}{L_c/2}\right)\right)^{1/2.4} \tag{12}$$

The semi-empirical formula of Savchenko (1998) also represents the cavity radius of each cavity section:

$$R_c(x) = R_n(2\sqrt{\frac{C_D}{\ln(1/\sigma)}}\frac{x}{R_n}-\frac{\sigma}{\ln(1/\sigma)}\frac{x^2}{R_n^2})^{1/2} \tag{13}$$

Fig. 3 shows different cavity shapes for various models, as determined according to the formulae proposed by Logvinovich (1972), Savchenko (1998), and May (1975), for σ =0.01,0.02, and 0.05.

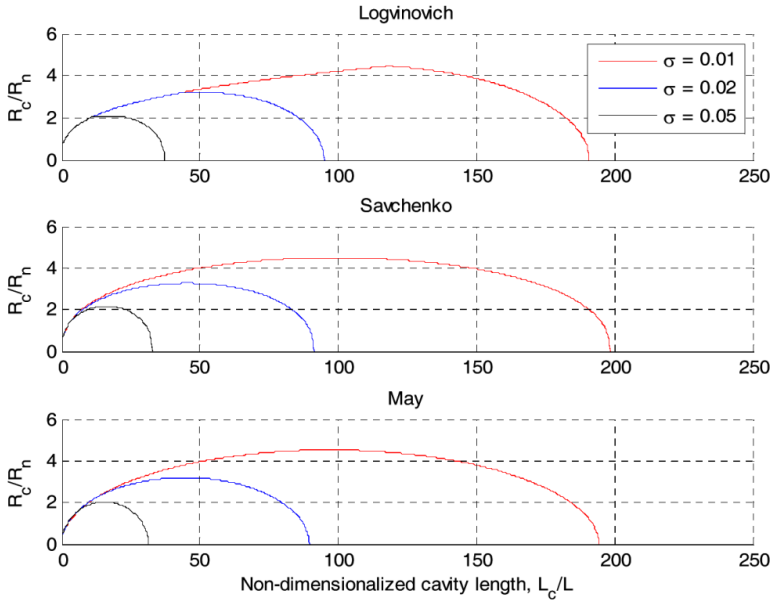

Fig. 3 Cavity profile according to different cavitation numbers.

Calculation of cavity axis

The cavitator continuously creates the cavity while the vehicle is moving. The cavity model described in the previous section is axisymmetric, and the cavity axis is equal to the trajectory of the cavitator. However, the cavity axis is distorted by the effects of gravity and the angle of attack of the cavitator. The effect of gravity on the cavity axis is characterized by a parameter called the Froude number, which is defined as the ratio of the flow velocity to the gravitational wave velocity as follows:

$$Fr_l = \frac{V_\infty}{\sqrt{gL_c}} \tag{14}$$

Here, F_{r_l} is the Froude number with respect to the cavity length L_c, and V_∞ is the flow velocity. The cavity axis is deformed in the upward direction (floating up of cavity tail) by gravity, and the effects are significant when the Froude number is relatively low; low Froude number implies "low velocity". The axis deformation can be determined by the momentum theorem (Logvinovich, 1972). The buoyancy force $\rho g V$ must be equal to the vertical momentum:

$$\dot{h}_g(x) = \frac{gQ(x)}{\pi V_\infty R_c^{\,2}(x)} \tag{15}$$

$$h_g(x) = \frac{g}{\pi V_\infty}\int_0^x \frac{Q(s)}{R_c^{\,2}(s)}ds \tag{16}$$

h_g is the upward deformation of the cavity axis with respect to the distance from the cavitator along the cavity axis, and $Q(x)$ is the cavity volume from 0 to x. More detailed modeling of the gravity effect was studied by Zou (2013). In Savchenko's work (Savchenko, 1998), an approximation formula was proposed:

$$h_g(x) = \frac{(1+\sigma)x^2}{3Fr_l^2} \tag{17}$$

The approximation formula is valid in the ranges $0.05 \le \sigma \le 0.1$ and $2.0 \le \mathrm{F}_{rl} \le 3.5$. Fig. 4 shows the cavity shape and cavity axis deformation by gravity obtained using Eq. (16). The x and y axis represent the non-dimensionalized cavity length and radius, respectively, for $F_{rl} = 10$ and $\sigma = 0.07$. Fig. 5 shows the comparison results of the cavity axis deformation calculated by Eqs. (16) and (17) for $F_{rl} = 2.5$ and $\sigma = 0.07$.

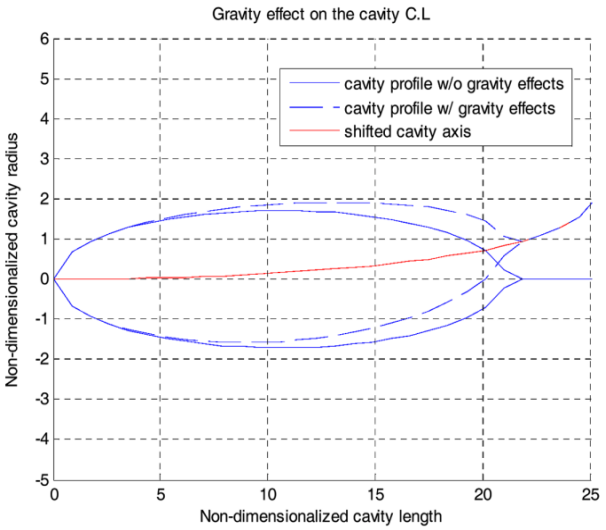

Fig. 4 Gravity effect on the cavity centreline.

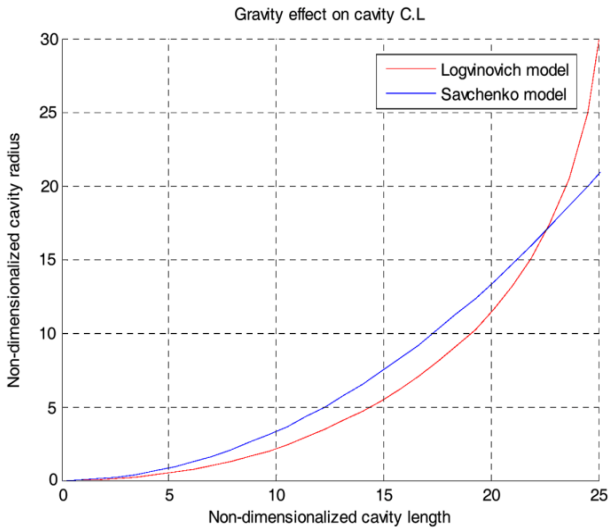

Fig. 5 Comparison of cavity centreline deformations.

The angle of attack of the cavitator also affects the cavity axis. The deformation is derived from Logvinovich's principle that the momentum generated by the cavitator must be equal and opposite to the momentum of the wake.

$$h_c(x) = -\frac{L_c}{\pi\rho V^2}\int_0^x \frac{ds}{R_c(x)^2} \tag{18}$$

Here, h_c is the deformation of the cavity axis along the cavity axis, and L_c is the lift force of the cavitator, which will be defined during the cavitator modeling. Fig. 6 shows the cavity axis deformation due to the angle of attack of the cavitator when the angle of attack = 15° and σ =0.02.

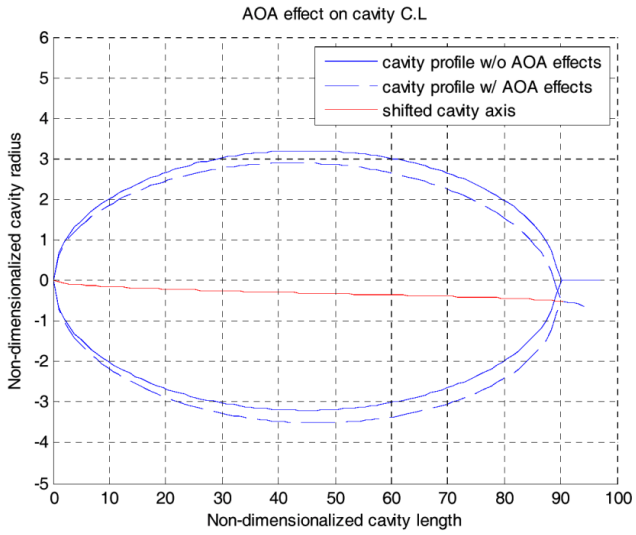

Fig. 6 Cavity axis deformation due to cavitator angle of attack; angle of attack = 15°, σ = 0.02.

The cavity shape and cavity axis were calculated because the immersion of the vehicle, which plays an important role in the hydrostatic/dynamic forces, is determined by the relative position between the cavity and vehicle. Fig. 7 shows the delayed cavity section. The vehicle immersion can be calculated from the location of the cavity center at the fin, X_{cavity}, and the cavity radius. Let $X_{cavitator}(t)$ be the present cavitator position and τ be the time for the cavity to reach the position of the fins. The position of the cavitator at the time $t-\tau$ in the earth-fixed frame can be written as follows:

$$X_{cavitator,E}(t-\tau) = X_{c.g,E}(t-\tau) + R_{B\to E}(t-\tau)\begin{bmatrix} l_{cav} \\ 0 \\ 0 \end{bmatrix} \tag{19}$$

$X_{cavitator,E}$ and $X_{c.g,E}$ are the cavitator location and center of gravity in the inertial frame; l_{cav} is the distance between the center of gravity and cavitator; and $R_{B\to E}$ is the rotation matrix from the body frame to the earth-fixed frame.

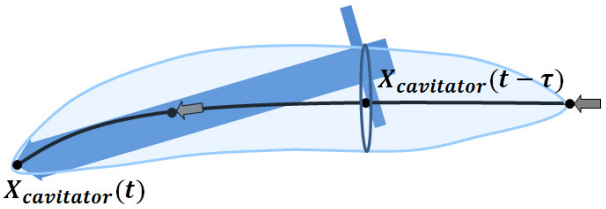

Fig. 7 Delayed cavity section.

The cavity center location at fin, X_{cavity}, is on the trajectory of the cavitator if there are no influences from gravity and the angle of attack. The cavity center location in Equ. (19) can be changed as follows by including the effects of gravity and the angle of attack.

$$\begin{aligned} X_{cavity,E}(t) &= X_{\text{cavitator},E}(t-\tau) + \text{gravity effect} + \text{A.O.A effect} \\ &= X_{\text{cavitator},E}(t-\tau) + \begin{bmatrix} 0 \\ 0 \\ h_g(t,\tau) \end{bmatrix} + \begin{bmatrix} 0 \\ h_{c,y}(t,\tau) \\ h_{c,z}(t,\tau) \end{bmatrix} \end{aligned} \tag{20}$$

Here, $X_{cavity,E}$ is the location of the cavity center at the fin in the inertial frame, and $h_{c,y}$ and $h_{c,y}$ are the y- and z-axis deformations, respectively, due to the angle of attack of the cavitator. As the cavity may be vertically deformed due to the time delay of the cavity generated at the cavitator, the horizontal deformation of the cavity axis can be addressed by the horizontally delayed cavity section. However, there is no gravity effect in the horizontal plane and the cavity axis deformation by centrifugal force is assumed to be negligible because the momentum of the fluid around cavity is not changed by centrifugal force.

Cavitator model

The cavitator is a fundamental part of the vehicle; it creates a cavity bubble around the body and generates forces and moments by changing the deflection angle to control the vehicle. The cavitator shape was assumed to be a disk that has a rotating motion only about the y-axis. The following relationships have been employed to estimate the drag and lift coefficients acting on the disk cavitator (May, 1975) in the flow axis:

$$C_D(\sigma,\alpha_c) \triangleq \frac{D_n(\sigma,\alpha_c)}{1/2\rho V_c^2 A_c} \cong C_{x0}(1+\sigma)\cos^2\alpha_c \tag{21}$$

$$C_L(\sigma,\alpha_c) \triangleq \frac{L_n(\sigma,\alpha_c)}{1/2\rho V_c^2 A_c} \cong C_{x0}(1+\sigma)\cos\alpha_c \sin\alpha_c \tag{22}$$

$$\begin{aligned} \alpha_c &= \tan^{-1}\left(\frac{w_c}{u_c}\right) + \delta_c \\ w_c &= w - q\cdot l_{cav} \end{aligned} \tag{23}$$

$$\begin{aligned} F_C &= [-D_n\cos\alpha_c - L_n\sin\alpha_c,\ 0,\ D_n\sin\alpha_c + L_n\cos\alpha_c]^T \\ F_{Cavitator} &= R_{C\to B}\cdot F_{Cavitator} \end{aligned} \tag{24}$$

where C_D and C_L are the drag and lift coefficients, respectively; D_n and L_n are the magnitudes of the drag and lift forces, respectively; F_C is the component of the cavitator force in the cavitator frame; $F_{Cavitator}$ is the component of the cavitator force in the body-fixed frame; $R_{C\to B}$ is the rotation matrix from the cavitator frame to the body frame; A_c is the disk area; V_c is the magnitude of the cavitator velocity with its component, $\begin{bmatrix} u_c & v_c & w_c \end{bmatrix}^T$, at the cavitator center expressed in the body-fixed frame; and α_c is the angle of attack calculated from the cavitator deflection angle δ_c and heave velocity. From (21)-(24), the lift and drag coefficients of the cavitator are functions of the angle of attack of the cavitator and cavitation number. The drag coefficient when the angle of attack was zero, C_{x0}, was determined from the experimental results of Kirschner et al. (2002). The frictional drag acting on the cavitator is negligible and the force about the added mass was calculated from Fan study (Fan et al., 2001).

Fin model

The four fins are located at the aft of the vehicle, and the location of the fin root from the center of gravity is defined as l_f. The horizontal fins are elevators while the vertical fins are rudders. The forces acting on the cavitating fins are complicated by the different flow regimes (Kirschner et al., 2002). At a low cavitation number, which is the supercavitating state, the cavity develops at the fin base. At a moderate cavitation number, a partial cavity develops at the leading edge of the fins separate from the base cavity. It was assumed that the fins have a wedge cross section and that the coefficients of the fin force and moment vary with the angle of attack of the fin (α_f) and the immersion depth (d_f). The coefficients were determined by interpolating the data provided by Kirschner et al. (2002). The forces and moments generated by the fin are given in fin coordinates as follows:

$$F_{f_i} = \frac{1}{2}\rho V_{f_i}^{\ 2} S_f^{\ 2} \begin{pmatrix} C_x(\alpha_{f_i}, d_{f_i}) \\ C_y(\alpha_{f_i}, d_{fi}) \\ C_z(\alpha_{fi}, d_{f_i}) \end{pmatrix} \tag{25}$$

$$M_{f_i} = \frac{1}{2}\rho V_{f_i}^{\ 2} S_f^{\ 3} \begin{pmatrix} C_{mx}(\alpha_{f_i}, d_{f_i}) \\ C_{my}(\alpha_{f_i}, d_{f_i}) \\ C_{mz}(\alpha_{f_i}, d_{f_i}) \end{pmatrix} \tag{26}$$

The terms $\left(C_x,\ C_y,\ C_z\right)$ are the fin force and moment coefficients, $\left(C_{mx},\ C_{my},\ C_{mz}\right)$, expressed in fin coordinates, as shown in Fig. 8. The subscript $i = 1,2,3,4$ refers to each fin; V_{fi} is the velocity of each fin in fin coordinates; and S_f is the fin span length. In this paper, the coordinate origins of the fin are located at the center of the hydrodynamic force acting on the fin (middle of the fin immersion). Therefore, the coordinate origin of the fin varies with its immersion depth and moments in fin coordinate. The forces and moments in each fin coordinate are transformed to the body-fixed coordinate using the rotation matrix as follows:

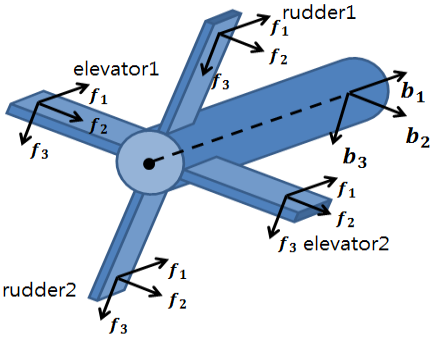

Fig. 8 Fin coordinate system.

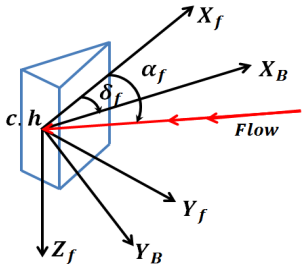

Fig. 9 Angle of attack and deflection angle of fin.

$$F_{fins} = \sum_{i=1}^{4} R_i F_{f_i} \tag{27}$$

$$M_{fins} = \sum_{i=1}^{4} (\vec{r_i} \times (R_i F_{f_i}) + R_i M_{f_i}) \tag{28}$$

where R_i is the rotation matrix from the fin coordinate i to the body-fixed coordinate, which is determined by the fin deflection angle δ_f, and $\vec{r_i}$ is the moment arm between the coordinate origin of each fin and the center of gravity.

Fig. 9 shows the relationships between the fin coordinate and body-fixed coordinate, where δ_f and α_f are the deflection angle and angle of attack of the fin, respectively.

The angle of attack of the fin can be calculated from the deflection angle of the fin and velocity in fin coordinates as follows:

$$V_f = \begin{bmatrix} u_f \\ v_f \\ w_f \end{bmatrix} = \begin{bmatrix} u \\ v \\ w \end{bmatrix} + \begin{bmatrix} 0 & -r & q \\ r & 0 & -p \\ -q & p & 0 \end{bmatrix} \vec{l}_{fin} \tag{29}$$

$$\begin{aligned} \alpha_{f,rudder} &= \arctan(\mathrm{v}_f / u_f) + \delta_{rudder} \\ \alpha_{f,elevator} &= \arctan(\mathrm{w}_f / u_f) + \delta_{elevator} \end{aligned} \tag{30}$$

where V_f is the velocity vector at the coordinate origin of the fin, expressed in body-fixed coordinates, and $\vec{l}_f$ is the position vector from the center of gravity to the coordinate origin of the fin.

Immersion depth

When a part of the fin is immersed, two types of forces act on the fin. The part of the fin that is immersed outside the cavity boundary generates forces and moments calculated using Eqs. (25) and (26), respectively. However, the non-immersed part of the fin, which is inside the cavity boundary, cannot generate as high forces and moment as the immersed part, because the fluid composition is a mixture of water and air. For simplicity, it is assumed that the non-immersed part of the fin does not generate forces and moments. As shown in Fig. 10, the fin immersion depth is calculated by using the cavity radius, which was described previously in the cavity model, and the location of the cavity axis ($X_{cavity,E}$), which can be calculated from (20), at the point where the fins are located.

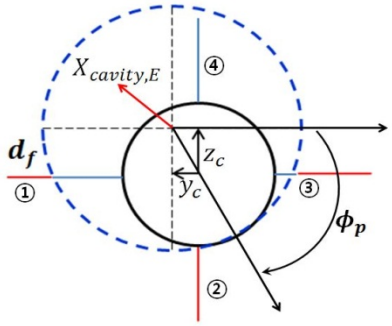

Fig. 10 Relative position of vehicle and cavity axis for calculating fin immersion depth.

The immersion of fin is calculated by Vanek's method (Vanek, 2008). In Fig. 10, d_f is immersion depth, y_c and z_c are offset values which are position vector from cavity center to body center in the inertial frame. The fins are numbered following the positive direction convention starting with the starboard fin at $\phi_1 = 0$ and each fin is at 90 degrees increment.

$$\phi_i = (i-1)\cdot\pi/2, \quad i = 1..4 \tag{31}$$

Then, the fin immersion depth (d_f) of each fin is as follows.

$$\begin{aligned}
&\bar{d}_{f,i} = \left[(S_f + R) - (y_c\cos(\phi_i) - z_c\sin(\phi_i)) - \sqrt{R_c^2 - (y_c\sin(\phi_i) + z_c\cos(\phi_i))^2}\right] / S_f \\
&Sat(\bar{x}) = \begin{cases} \bar{x} & if \quad 0 \le \bar{x} \le 1 \\ 0 & if \quad \bar{x} < 0 \\ 1 & if \quad \bar{x} > 0 \end{cases} \\
&d_{f,i} = Sat(\bar{d}_{f,i})
\end{aligned} \tag{32}$$

Likewise, the immersion depth of the body can be calculated in the same manner.

$$h_0(t,\tau) = \begin{cases} \sqrt{y_c^2 + z_c^2} - R_c + R & if \quad \sqrt{y_c^2 + z_c^2} > R_c - R \\ 0 & if \quad \sqrt{y_c^2 + z_c^2} \le R_c - R \end{cases} \tag{33}$$

The direction of immersion relative to the body y-axis is defined as:

$$\phi_p = \tan^{-1}(z_c / y_c) \tag{34}$$

Forces acting on wetted body

For the partially cavitating case, the vehicle body extends beyond the cavity closure point. In this stage, hydrostatic and hydrodynamic forces are acting on the wetted area of the body including the added mass. In the fully developed cavity stage (supercavitating condition), the cavity extends the body dimensions, and therefore the forces are acting only on the control surface, such as fins and cavitator. In this case, the added mass is only acting on the cavitator. The wetted area and volume of the body can be easily calculated by utilizing the cavity profile. The hydrostatic forces and moments are the buoyancy forces and moments as calculated by (35) and (36), respectively.

$$F_B = \begin{bmatrix} -B_{wet}\sin\theta \\ B_{wet}\cos\theta\sin\phi \\ B_{wet}\cos\theta\cos\phi \end{bmatrix} \tag{35}$$

$$M_B = \begin{bmatrix} y_b B_{wet}\cos\theta\cos\phi - z_b B_{wet}\cos\theta\sin\phi \\ -z_b B_{wet}\sin\theta - x_b B_{wet}\cos\theta\cos\phi \\ x_b B_{wet}\cos\theta\sin\phi + y_b B_{wet}\sin\theta \end{bmatrix} \tag{36}$$

here, (ϕ,θ,ψ) are the Euler angles; B_{wet} is the magnitude of the buoyancy and given by $B_{wet} = \rho g V_{wet}$; and $X_{buoy} = [x_b\ y_b\ z_b]^T$ is the position vector from the center of gravity to the center of buoyancy.

The hydrodynamic forces acting on the wetted area are the pressure drag, frictional drag, and forces caused by the added mass. The hydrodynamic forces are calculated in two directions: X_B-axis and Y_B, Z_B-axis. This is because a supercavitating vehicle has the same sectional shape for the hydrodynamic forces as those acting along the Y_B and Z_B-axes. Fig. 11 shows the hydrodynamic forces acting on the X_B-axis. The pressure drag and forces that are caused by the added mass and act on the cavitator are included in the cavitator model. The normal pressure contributions along the wetted body are assumed to have x-axis symmetry; further, it is assumed that the pressure drag exists only at the cavitator. The viscous contributions to the frictional drag coefficient (C_F) along the wetted portion of the body are calculated by using the Hughes line for the friction coefficient (Newman, 1977); thus, (37) expresses the frictional drag on the wetted body.

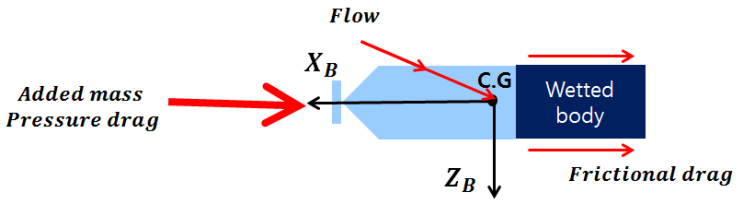

Fig. 11 Hydrodynamic forces acting on X_B-axis.

$$D_F = \frac{1}{2}\rho S_{wet} u^2 C_F$$
$$C_F = \frac{0.075}{(\log_{10}\mathrm{Re} - 2)^2} \tag{37}$$

D_F is the magnitude of the friction drag that acts in the negative direction of the forward speed of the body; Re is the Reynolds number; and ρ is the fluid density. The frictional drag force expressed in body-fixed coordinates can be written as follows:

$$F_{Friction} = \begin{bmatrix} -D_F \cdot (1 - \frac{DR}{100}) \\ 0 \\ 0 \end{bmatrix} \tag{38}$$

Drag reduction (DR) is the percentage of the frictional drag reduction. If the fluid is a mixture of water and gas, the density of the fluid can be attributed to the bubble and water. In this study, the friction drag is calculated using the water density, and the DR caused by the bubbles is addressed in the next section.

The hydrodynamic force acting on the $Y_B - Z_B$ plane ($F_{Morison}$) is calculated by Morison's equations (Newman, 1977) as follows (Eqs. (39) and (40)):

$$F_{Morison} = F_I + F_D \tag{39}$$

$$dF_{Morison} = \rho C_m \pi R^2 \int \dot{\vec{V}}\, ds + \rho C_D R \int \vec{V}|V|\, ds \tag{40}$$

$F_{Morison}$ is calculated by integrating $dF_{Morison}$, which is the differential hydrodynamics force acting on the wetted part of the vehicle body. *ds* is the differential length along the X_B-axis; F_I is the force proportional to the acceleration; F_D is the force proportional to the square of the velocity, which is the sum of the friction drag and pressure drag; C_m and C_D are the added mass and drag coefficients-1 and 1.3, respectively-for the cylindrical section; and $\vec{V}$ and $\dot{\vec{V}}$ are the velocity and acceleration, respectively, of the flow in the $Y_B - Z_B$ plane relative to the body. The flow velocity distribution relative to the body is determined by the body pitch and yaw rate, and it is expressed in Eq. (41) and shown in Fig. 12 as the velocity distribution along the X_B-axis.

$$d\vec{V} = \begin{bmatrix} u \\ v \\ w \end{bmatrix} + \begin{bmatrix} 0 & -r & q \\ r & 0 & -p \\ -q & p & 0 \end{bmatrix} \begin{bmatrix} ds \\ 0 \\ 0 \end{bmatrix} \tag{41}$$

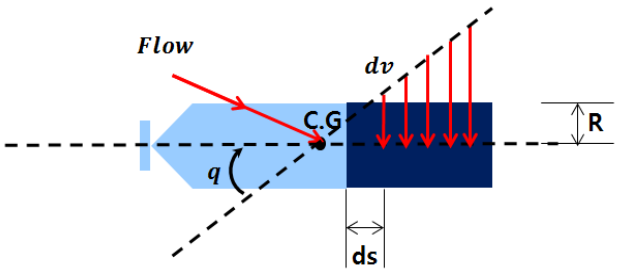

Fig. 12 Velocity distribution along the X_B-axis in wetted body.

The moment generated by the force in Eq. (39) can be written as follows:

$$M_{Morison} = \begin{bmatrix} 0 \\ l_{h.c} \cdot F_{Morison,z} \\ -l_{h.c} \cdot F_{Morison,y} \end{bmatrix} \tag{42}$$

where $l_{h.c}$ is the distance from the center of gravity to the hydrodynamic center of $F_{Morison}$ along the X_B-axis; and $F_{Morison,y}$ and $F_{Morison,z}$ are the Y_B- and Z_B-axes components, respectively, of $F_{Morison}$.

The total forces and moments acting on the wetted body can be written as follows:

$$F_{wet} = F_B + F_{Morison} + F_{friction} \tag{43}$$

$$M_{wet} = M_B + M_{Morison} \tag{44}$$

Planing force model

The planing of the body on the cavity generates forces and moments. The planing force is the interaction force between the vehicle transom and cavity wall. The planing force model has been investigated by Logivinovich (1980) and Vasin and Paryshev (2001). In this paper, Paryshev's model is employed since it was shown to fit the experimental data better (Dzielski, 2006). Fig. 13 shows the planing of a body on the cavity wall. The coordinate ζ is at a distance along the X_B-axis from the transom. α_p is the planing angle and h_0 is the immersion depth when $\zeta = 0$; it is the maximum immersion depth. The apparent mass per unit length can be calculated by using Eq. (45).

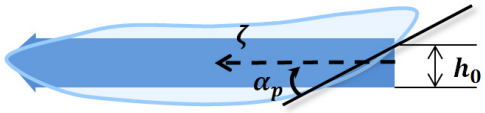

Fig. 13 Planing of body on cavity wall.

$$m_p^*(h) = \pi\rho R^2 \left(1 - \left(\frac{\Delta}{(\Delta + h)}\right)^2\right) \tag{45}$$

here, Δ is a gap between the body and cavity radius: $\Delta = R_v - R$. h is the immersion depth. Using the apparent mass per unit length, Dzielski (2011) expressed the magnitude of planing force as follows:

$$-F_p = M^* \dot{w}_T + \frac{\partial M^*}{\partial h_0} w_T^2 \tag{46}$$

here, w_T is the transom velocity, which is equal to the immersion velocity of the body into the cavity wall, and M^* is the apparent mass expressed as follows:

$$\begin{aligned} M^* &= \int_0^{h_0/\tan\alpha_p} m^*(h) d\zeta \\ &= \int_0^{h_0/\tan\alpha_p} m^*(h_0 - \zeta\tan\alpha_p) d\zeta \\ &= \pi\rho R^2 \frac{h_0^2}{(\Delta + h_0)\tan\alpha_p} \end{aligned} \tag{47}$$

The planing moment can be obtained by calculating the center of pressure of the planing force, x_p

$$x_p = \frac{h_0(\Delta + h_0)}{2(\Delta + h_0)\tan\alpha_p} \tag{48}$$

The direction of planing force and moment can be described using the direction of immersion of body ϕ_p in Eq. (34). In this planing model, several conditions are assumed-the constant immersion velocity, instantaneous cavity formation, the steady planning, and a positive small value of the gap. The shape of the cavity surface where the immersion occurs is assumed to be cylindrical. For the planing with noncylindrical cavity, see the Nguyen's study (Nguyen, 2011).

NUMERICAL SIMULATIONS

Numerical simulations of the integrated model were performed to analyze the characteristics of the system and validate the modeling. The vehicle parameters are shown in Table 1; it is based on the benchmark high-speed supercavitating vehicle model used by Dzielski and Kurdila (2003). The body has a uniform density ρ_b, and the ratio of body density to water density is $m = \rho_b / \rho$. The vehicle mass M, the moment of inertia relative to the cavitator-fixed frame, I_{yy}, and the location of the center of gravity relative to the cavitator, x_g, can be expressed as follows:

$$M = \frac{7}{9}(m\rho\pi)R^2L \tag{49}$$

$$I_{yy} = \frac{11}{60}(m\rho\pi)R^4L + (m\rho\pi)R^2L^3 \tag{50}$$

$$x_g = -\frac{17}{28}L \tag{51}$$

Table 1 System parameters for vehicle model

Parameters	Description	Value and units
g	Gravitational acceleration	$9.81\ m/s^2$
m	Density ratio (ρ_b / ρ)	2
R_n	Cavitator radius	$0.0191\ m$
R	Vehicle radius	$0.0508\ m$
S_f	Fin span length	$0.1\ m$
L	Vehicle length	$1.8\ m$
C_{x0}	Drag coefficient	0.82

Scenario 1 : vertical open-loop simulation

Fig. 14 shows the open-loop time response of the integrated model. The simulation conditions are shown in Table 2. The variables shown in the figure are vertical plane variables because the lateral plane variables are constant and equal to zero. Here, X_E and Z_E positions, respectively, in the earth-fixed frame and *u* and *w* are the velocities, respectively. θ is the pitch angle and *q* is the angular velocity in pitch.

In initial stage, especially before 1 second, the pitch angle of the vehicle negatively increases because the fins (elevators in this case) and the cavitator generate negative pitch moment. The forward speed is always positive due to the thrust force, and the heave velocity is also always positive due to the gravity force. Therefore, the angle of attack of the cavitator and the Z_B-axis force are positive according to Eqs. (23) and (24), respectively, and the cavitator generates negative pitch moment. Similarly, the fins generate negative lift force and moments.

There is unstable regime around 1 second. In that regime, the cavity is developed beyond the fin root and fin (rudder in this case) immersion depth is changed (not zero). Asymmetry of immersion depth, which is caused by gravity effect on the cavity axis, makes asymmetric drag force and pitch moment. The unstable pitch moment is disappear when the cavity size is decrease as depth increases.

Fig. 15 shows the cavity radius and length according to the cavitation number. In the initial stages, the cavitation number is relatively small and the cavity is developed. The growth of the cavity reduces the wetted area of the body as well as the frictional drag. Therefore, the forward speed u rapidly increases in the initial state. The drag coefficient of the cavitator has a minimum value when the cavitation number is zero and increases with cavitation number (Eq. (21)). The maximum drag coefficient, $C_{D,\max}$ is 1.17 in this paper, which is identical to the disk drag coefficient in water. Hence, the forward speed converges to a constant value (approximately 90 *m/s*), and the drag coefficient reaches its maximum value.

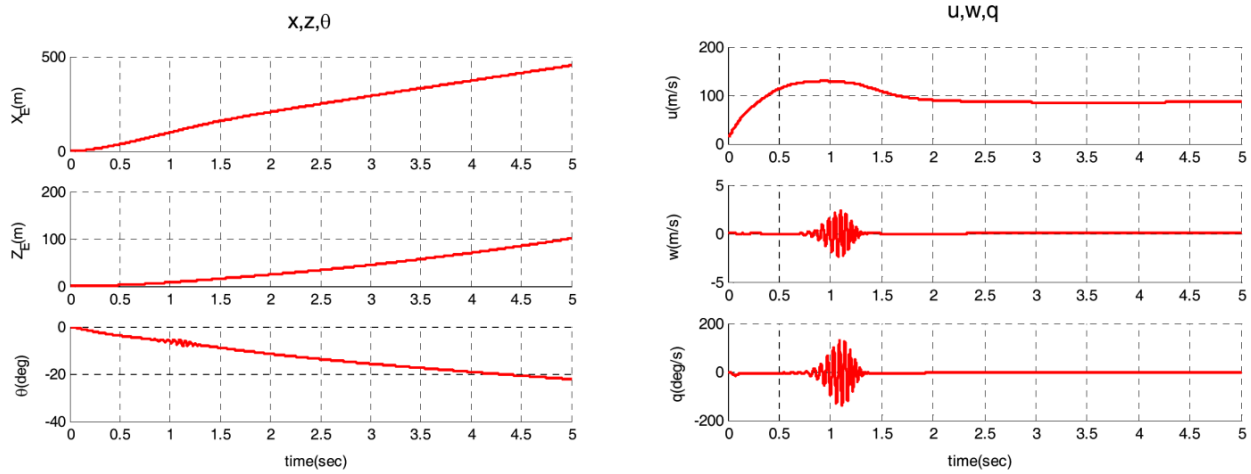

Fig.14 Vertical open-loop simulation results of the integrated model.

Table 2 Conditions for vertical open loop simulation.

State	Description	Value
T	Magnitude of thrust force	9000 *N*
z_0	Initial depth	1 *m*
u_0	Initial forward velocity	10 *m/s*
δ_c	Cavitator deflection angle	0 *deg.*
δ_e	Elevator deflection angle	0 *deg.*
δ_r	Rudder deflection angle	0 *deg.*

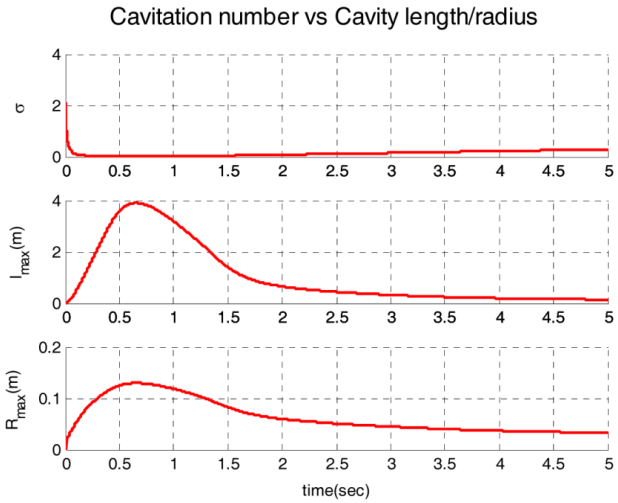

Fig. 15 Cavity profile versus cavitation number.

Scenario 2 : lateral open-loop simulation

In lateral open loop simulation, of which conditions are same as in Table 2 except the rudder deflection angle (δ_r). The rudder deflection angle is changed from 0 to 0.65 *deg.* at 1 second

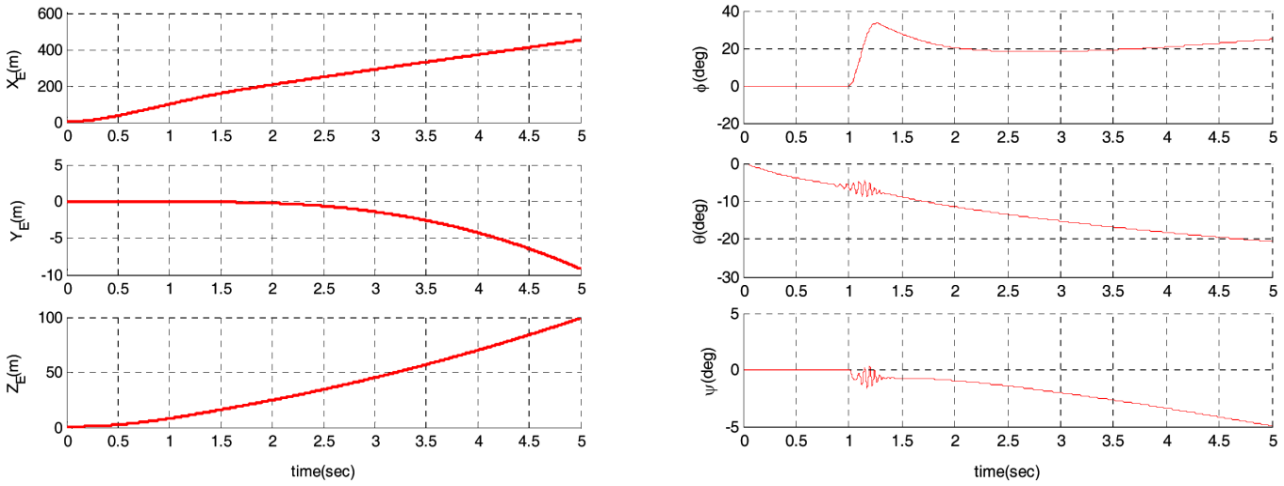

Fig. 16 Lateral open-loop simulation results, position and Euler angle.

here, X_E, Y_E and Z_E are positions, respectively, in the earth-fixed frame and ϕ, θ and ψ are Euler angle. *u*, *v* and *w* are the velocities, respectively, in the body-fixed frame and *p*, *q* and *r* are the angular velocities. The rudder force and moment are generated due to the rudder deflection angle (δ_r) after 1 second. As seen in Fig. 17, the variables associated with lateral dynamics such as *v, p, r* are zero before 1 second. The rudder generates force in Y_B-axis and yaw moment. The roll angle also increases because the longitudinal and lateral dynamics are coupled. Roll angle (ϕ) is bigger than yaw angle (ψ)

Because X_B-axis moment of inertia (I_{xx}) is much smaller than the Z_B-axis moment of inertia (I_{zz}).

Fig. 18 shows the cavity axis offset from X_B-axis calculated by Eq. (20) and the vehicle position. Fig. 19 shows the direction of immersion calculated by Eq. (34) and magnitude of planing force/moment. Before 1 second, there is only vertical distance (Z_c) between cavity axis and vehicle centerline due to the gravity effect. The fin and body immersion depth are calculated by the offset values by Eqs. (32)-(33). The vertical offset (Z_c) has relatively large value in initial phase, where the gravity effect is significant when the Froude number is relatively low; low Froude number implies "low velocity". In that phase, the direction of immersion is $\pm\pi/2$.

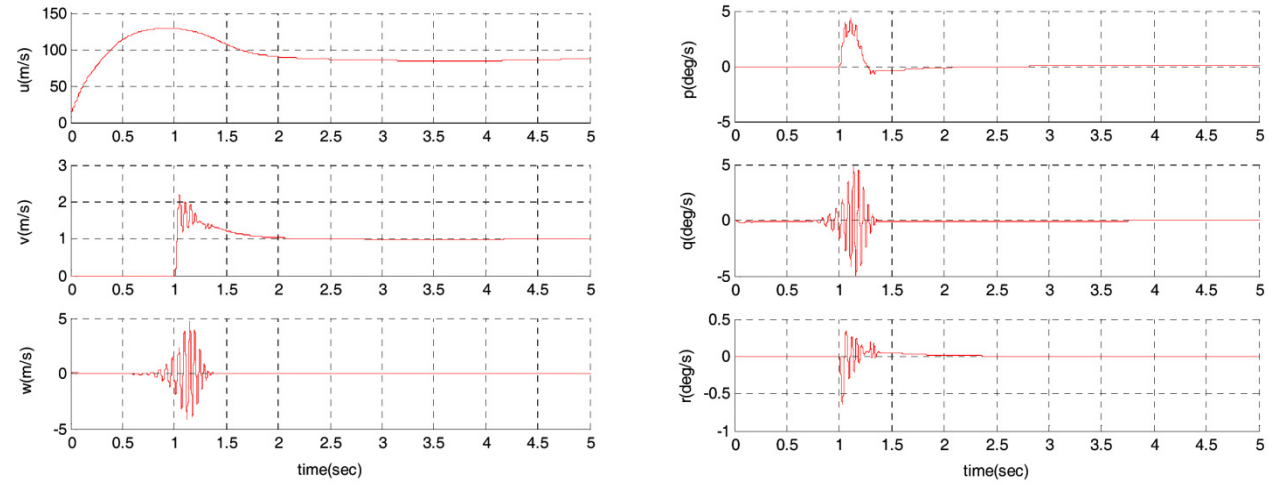

Fig. 17 Lateral open-loop simulation results, linear and angular velocities.

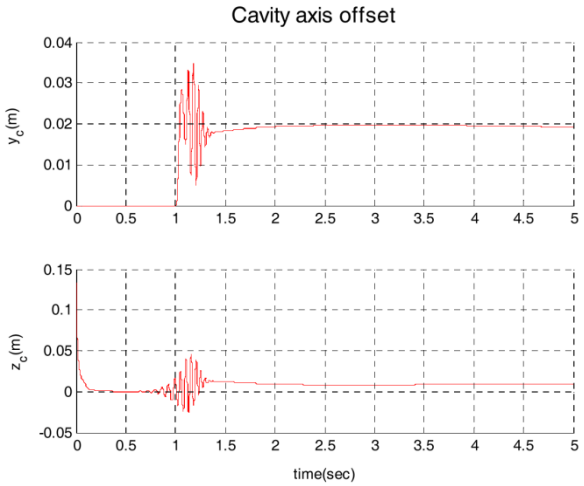

Fig. 18 Cavity axis offset from X_B-axis.

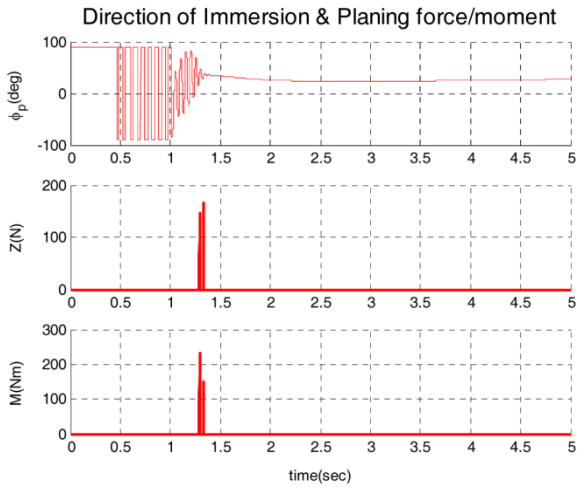

Fig. 19 Direction of Immersion and Planing force/moment.

In both cases of simulation oscillatory responses are present around one second. The oscillatory response has nothing to do with the deflection of rudders, but it is due to the longitudinal asymmetry of forces exerted on the upper rudder and the lower rudder. Because of the effect of gravity, the cavity is deformed astern upward. Larger drag force exerted on the lower rudder than on the upper rudder generates negative (nose-down) pitching moment, which in turn immerses the upper rudder and produces more drag force than the lower rudder, and engenders positive pitching moment. This phenomenon would repeat and may destabilize the system as long as the cavity could maintain its size and length. However, the simulation results in Figs. 14-19 show that the oscillatory response dies out in a short period of time as the depth of the vehicle gets deeper. The cavitation number which is a function of the depth and speed of a vehicle increases and the size of the cavity is reduced. The sensitive response of the vehicle is quickly suppressed as the cavity contracts. The cavity is reduced to be partial cavity that does not reach the location of the rudders, and the asymmetric drag force on the rudders disappears.

CONCLUSIONS

In this study, we performed integrated dynamics modeling of a supercavitating vehicle. A 6-DOF equation of motion was constructed by defining the forces and moments acting on the supercavitating body. Each part of the vehicle was modeled by referring to previous researches, and we integrated the different models to obtain the dynamics of a supercavitating system. The cavity modeling consisted of calculations involving the size of the cavity and cavity axis. The wetted area of each part of the vehicle was defined based on the cavity model. Subsequently, by using the integrated dynamics model, we conducted numerical simulations to analyze the characteristics of the supercavitating system and validate the modeling completeness. The simulation results demonstrated that the vehicle is unstable when the fin immersion depth is asymmetric and dynamics of horizontal & vertical is coupled. Depth control is required to maintain the supercavitating condition, and moreover, the flight envelope should be determined. Our research results can be used for understanding and employing supercavitating vehicle systems. Further, based on this research, high-quality controllers and optimal supercavitating systems can be designed, and the specifications of components such as ventilation systems, cavitators, or fins can be efficiently chosen.

ACKNOWLEDGMENT

This research was supported by Basic Science Research Program through the National Research Foundation of Korea (NRF) funded by the Ministry of Education, Science and Technology (NRF-2012R1A1A2008633).

REFERENCES

Ahn, B.K., Lee, T.K., Kim, H.T. and Lee, C.S., 2012. Experimental investigation of supercavitating flows. *International Journal of Naval Architecture and Ocean Engineering*, 4(2), pp.123-131.

Dzielski, J. and Kurdila, A., 2003. A benchmark control problem for supercavitating vehicles and an initial investigation of solutions. *Journal of Vibration and control*, 9(7), pp.791-804.

Dzielski, J.E., 2006. Experimental validation of planing models for supercavitating vehicles. *Proceedings of Undersea Defense Technology Pacific Symposium*, San Diego, CA, USA, 6-8 December 2006.

Dzielski, J.E., 2011. Longitudinal stability of a supercavitating vehicle. IEEE Journal of *Oceanic Engineering*, 36(4), pp. 562-570.

Elbing, B.R., Winkel, E.S., Lay, K.A., Ceccio, S.L., Dowling, D.R. and Perlin, M., 2008. Bubble-induced skin-friction drag reduction and the abrupt transition to air-layer drag reduction. *Journal of Fluid Mechanics*, 612, pp.201-236.

Fan, H., Zhang, Y. and Wang, X., 2011. Longitudinal dynamics modeling and MPC strategy for high-speed supercavitating vehicles. *In Electric Information and Control Engineering (ICEICE), 2011 International Conference on IEEE*, Wuhan, China, 15 - 17, Apr, 2011, pp.5947-5950.

Fine, N.E., Uhlman, J.S. and Kring, D.C., 2001. *Calculation of the added mass and damping forces on supercavitating bodies*. [online] Avaliable at : <http://resolver. caltech. edu/cav2001: sessionB3. 006> [Accessed 20 March 2014].

Garabedian, P.R., 1956. Calculation of axially symmetric cavities and jets. *Pacific Journal of Mathematics*, 6(4), pp.611-684.

Hassouneh, M.A., Nguyen, V., Balachandran, B. and Abed, E.H., 2013. Stability Analysis and control of supercavitating vehicles with advection delay. *Journal of Computational and Nonlinear Dynamics*, 8(2), pp.021003.

Kirschner, I.N., Kring, D.C., Stokes, A.W., Fine, N.E. and Uhlman, J.S., 2002. Control strategies for supercavitating vehicles. *Journal of Vibration and Control*, 8(2), pp.219-242.

Li, D., Luo, K., Huang, C., Dang, J. and Zhang, Y.. 2014. Dynamics model and control of high-speed supercavitating vehicles incorporated with time-delay. *International Journal of Nonlinear Sciences and Numerical Simulation*, 15(3-4), pp.221-230.

Logvinovich, G., 1972. *Hydrodynamics of free-boundary flows, translated from Russian (NASA-TT-F-658)*. Washington D.C.: NASA.

Logvinovich, G. and Syeryebryakov, V.V., 1975. On methods of calculations of slender asymmetric cavities. *Gidromenhanika*, 32, pp.47-54.

Logvinovich, G.V., 1980. Some problems in planing surfaces. *Trudy TsAGI*, 2052, pp.3-12.

May, A., 1975. *Water entry and the cavity-running behavior of missiles, NAVSEA hydrodynamics advisory committee, Report.TR 75-2.* Silver Spring, Maryland: NAVSEA Hydrodynamics Advisory Committee.

Newman, J.N., 1977. *Marine hydrodynamics*. Massachusetts: MIT Press.

Nguyen, V. and Balachandran, B., 2011. Supercavitating vehicles with noncylindrical, nonsymmetric cavities: dynamics and instabilities. *Journal of Computational and Nonlinear Dynamics*, 6(4), pp.041001.

Park, S. and Rhee, S.H., 2012. Computational analysis of turbulent super-cavitating flow around a two-dimensional wedge-shaped cavitator geometry. *Computers and Fluids*, 70, pp.73-85.

Savchenko, Y.N., 1998. *Investigation of high speed supercavitating underwater motion of bodies, High-speed Motion in Water, AGARD Report 827, 20-1-20-12*, NASA 19980020552. Washington D.C: NASA.

Vanek, B., Bokor, J., Balas, G.J. and Arndt, R.E.A., 2007. Longitudinal motion control of a high-speed supercavitation vehicle. *Journal of Vibration and Control*, 13(2), p.159.

Vanek, B., 2008. *Control methods for high-speed supercavitating vehicles*. Doctoral dissertation. University of Minnesota.

Varghese, A.N., Uhlman, J.S. and Kirschner, I.N., 2005. Numerical analysis of high-speed bodies in partially cavitating axisymmetric flow. *Journal of Fluids Engineering*, 127(1), pp.41-54.

Vasin, A.D. and Paryshev, E.V., 2001. Immersion of a cylinder in a fluid through a cylindrical free surface. *Fluid Dynamics*, 36(2), pp.169-177.

Xiang, M., Cheung, S.C P., Tu, J.Y. and Zhang, W.H., 2011. Numerical research on drag reduction by ventilated partial cavity based on two-fluid model. *Ocean Engineering*, 38(17), pp.2023-2032.

Zou, W., Yu, K.P. and Wan, X.H., 2010. Research on the gas-leakage rate of unsteady ventilated supercavity. *Journal of Hydrodynamics, Ser. B*, 22(5), pp.78-783.